Experimental and Numerical Studies of a Triple Flame

P. N. KĪONI[†] AND K. N. C. BRAY
University of Cambridge, Department of Engineering, Cambridge CB2 1PZ, England

D. A. GREENHALGH
Cranfield University, School of Mechanical Engineering, Cranfield, Bedford MK43 OAL, England

B. ROGG*
Ruhr-Universität Bochum, Institut für Thermo- und Fluiddynamik, Lehrstuhl für Strömungsmechanik, D-44780 Bochum, Germany

The structure of a laminar triple flame is investigated both experimentally and numerically. The distribution of OH radicals in the flame is mapped using Laser Induced Fluorescence. The structure of the velocity field is mapped using Particle Imaging Velocimetry. To obtain detailed information on both the fields of velocity and scalars, the flame is numerically simulated. In the simulations, gas expansion is taken into account and the full Navier-Stokes equations are solved. Numerical results obtained with global one-step chemistry and, alternatively, with a detailed chemical kinetic mechanism are presented. The experimental findings are compared with the numerical results.

INTRODUCTION

Turbulent non-premixed or partially premixed flames provide an environment where locally and instantaneously combustion may take place in thin mixing layers. The spatial and temporal fluctuations in such flames may lead to local extinction due to excessive local straining. Since hot burnt gases may exist in the neighbourhood of unreacted mixture, re-ignition may occur when the flowfield conditions, expressed for instance in terms of the strainrate, are favourable. A combustion region within a turbulent flame such as the one just described is bound to have variations in the equivalence ratio of the mixture. Furthermore, non-premixed and partially premixed turbulent flowfields consist of regions with local variations of the equivalence ratio. In some of these regions, stoichiometries vary from lean to rich, thereby allowing triple-flame structures to develop. Since depending on flow conditions a turbulent flame may be viewed as an ensemble of laminar flamelets, [1–4], the modelling of non-premixed or partially premixed turbulent flames as an ensemble of laminar triple flamelets could be greatly facilitated by gaining detailed knowledge of the structure and propagation behaviour of laminar triple flames [5].

The triple flame structure was first observed by Phillips [6] in an experimental study of fire spread in buoyant methane-air mixing layers at the roof of coal mines. The initial focus of this early research was on the flame propagation speed in mixing layers of very small transverse mixture fraction gradient at the leading edge of the flame. Liñán and Crespo [7] used large-activation-energy-asymptotics to study the internal structure of a flame propagating in a direction generally perpendicular to the isopleths of a mixing layer. It was shown that behind an initial deflagration of a premixed flame, the excess oxidizer and fuel from the lean and the rich sides, respectively, of the region of stoichiometric mixture are consumed in a diffusion flame. Dold [8–10] has extended this study to include upstream heat conduction, hence upstream flame propagation, and has studied, using a thermal-diffusional model, the dependence of flame propagation on the mixture fraction gradient in the region of stoichiometric mixture. Using a similar model, Kīoni et al. [11] studied numerically the response to strain of the structure and propagation velocity of a triple flame in a counterflow configuration.

In this paper, a study of the structure of the flowfield upstream of a triple flame and of the internal structure of the flame is presented. In

*Corresponding author.
[†]Present address: Department of Mechanical Engineering, Jomo Kenyatta University, P.O. Box 62000, Nairobi, Kenya.

0010-2180/99/$19.00
PII S0010-2180(98)00035-2

particular, the work presented is a continuation of the experimental and numerical work reported by Kīoni et al. [11]. In the following section, experimental work is presented in which the distribution of the hydroxyl radicals in the flame and the velocity field upstream of, and in, the flame are mapped using Laser Induced Fluorescence (LIF) and Particle Imaging Velocimetry (PIV), respectively. In the following section, the numerical simulation of a triple flame propagating in a geometry similar to that of the experimental work is presented. The numerical model uses variable density and therefore solves the full Navier-Stokes equations. A simple one-step chemistry model and alternatively a short detailed mechanism of elementary chemical reactions is employed in the simulations to provide detailed information on the structure of the species mass fraction fields.

EXPERIMENTAL STUDIES

Apparatus

The triple flame is generated in the experimental rig described in detail by Kīoni et al. [11]. Thus, the flame is stabilized in a free stream of laminar flow, away from any obstacles and in a vertical orientation. The flame is insulated from the walls on all four sides by coflowing streams of inert gas and non-flammable air-fuel mixture. The mixture fraction far upstream of the flame in the plane of the triple flame structure varies linearly in the direction perpendicular to the flow direction. Some minor modifications, which will be described below as appropriate, were made to the rig to enable the measurements to be made.

OH laser induced fluorescence.

To facilitate LIF measurements of the OH radical, the modifications included connecting a seeder in the fuel line upstream of the burner in order to seed the flow with acetone vapour. The purpose of the acetone was to provide images needed in the normalization of the OH-LIF images. Polished fused silica windows through which the laser beam and the collected beams pass, so as to eliminate secondary fluorescence which may occur at the windows, were also introduced. The LIF imaging of OH was done at 308 nm. A tunable XeCl pulsed laser, Lambda Physik Model 150 MSC, capable of generating single pulses of 20 nsec duration, at a maximum frequency of 80 Hz and at a maximum power of 180 mJ per pulse, is used as the source. The laser sheet condition provided a total photon count per image, which linearly varied as a function of the laser energy per pulse. During recording of the images the laser energy per pulse was 110 J, and it was attenuated by a factor of 6. The energy of the laser sheet was far below that required to saturate the excitation.

The optical arrangement is illustrated in Fig. 1. The laser beam is formed into a collimated laser sheet, approximately 60 mm high and of a thickness of approximately 0.1 mm, using a spherical lens of focal length 2.0 m and two cylindrical lenses of focal lengths 75 and 150 mm, respectively. Suitable mirrors conveniently direct the focused beam to the burner at a suitable height and orientation.

The collection optics are focused perpendicularly on the laser sheet to image an area approximately 40 mm wide and 70 mm high, thus encompassing the front area of the triple flame. A Nikkor uv lens, F110 mm f4.5, focuses the image onto a gated MCP Image intensifier. A narrow bandbass filter, centered at 308 nm, is placed in front of this lens to eliminate undesired light from the collected beam. The gated intensifier provides the photon intensification of the image and also operates as a fast camera shutter. The intensifier is run using a Princeton Instruments PG200 unit which also provides the synchronization between the laser firing and the intensifier gating. A gate time of 200 nsec, small enough to virtually eliminate light from the surroundings, is used. A front-to-front Pentax lens, F50 mm f1.2, focuses the intensified image on a CCD which has a detector array of 400 by 600 pixels. Images from the CCD camera were first stored and sorted on a PC, but for further analysis they were transferred to a DEC station 3100.

Fluorescence of the OH radicals was collected for unsaturated excitation. Consequently, the fluorescence images had to be corrected for the laser sheet structure in addition to correcting for the spatial structure of the collection optics. The normalization images are obtained

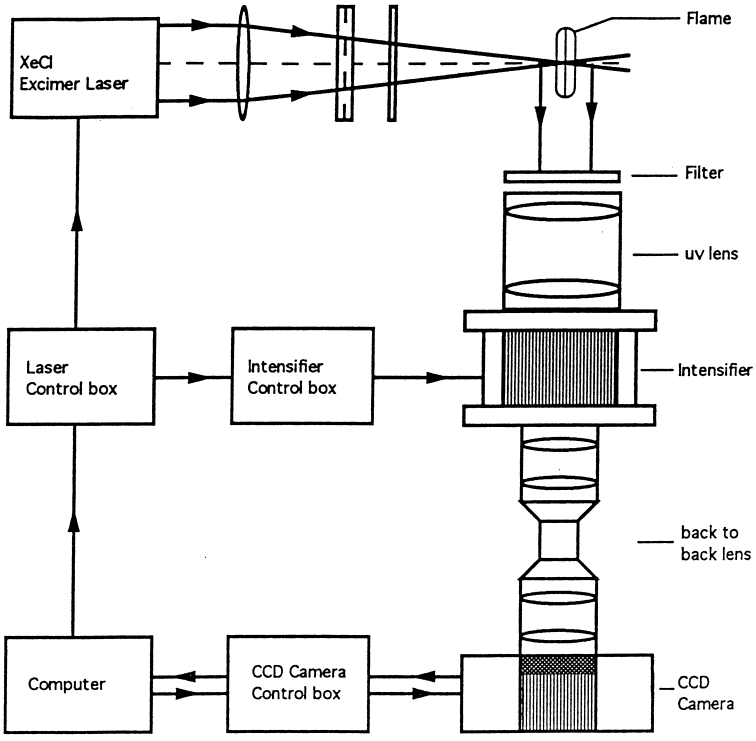

Fig. 1. Arrangement of the optical apparatus for imaging OH Laser Induced Fluorescence.

by collecting the fluorescence of a uniform flow in the burner of nitrogen seeded with acetone, using the same optical settings. The background images are obtained by recording the fluorescence of the flame at off-resonant excitation, for the OH background images, and imaging the carrier gas only, for the background images for the normalization images. To reduce the level of noise in the recorded images, mean images, typically 20 for every recorded image, are collected in a second.

Particle imaging velocimetry.

For PIV measurements a procedure, which is described in detail in [12], was developed for seeding the flow with solid particles in such a way that the velocity and the mixture fields are largely preserved. Zirconium dioxide powder, with particle sizes in the range 5–9 μm, was selected because of its good scattering cross-section, both at the low and the high temperatures encountered in the flame. In addition, particles from this powder do not interfere with the combustion process and were found to agglomerate much less than alternative markers such as titanium dioxide.

The source of the illumination is a Nd:Yag laser with its fundamental wavelength doubled to 532 nm. Double pulses have a maximum separation time of 1.0 ms, each pulse being of a duration of 10 nsec and a power of 120 mJ. A spherical and a cylindrical lens form the laser sheet into a sheet of thickness 0.5 mm at line of focus and a height of 60 mm. Hence, the laser sheet is focused on the burner to cover the area of the triple flame structure and the region upstream of it. The laser sheet thickness in the burner is of the order of 0.1 mm.

For a pair of laser pulses, the particle image pairs are captured on a 35 mm TMAX ASA 3200 photographic film using a Micro-NIKKOR lens F105 f2.8 focused on the laser sheet in the burner. Subsequently, a frame of the developed photographic film is individually analyzed using numerical autocorrelation, presented in detail by Armstrong [13], to determine the structure of the velocity field.

Design and operation of the burner is such that the velocity of the flow at the inlet to the combustion chamber is uniform. This was validated using hot-wire anemometry. In the PIV study, for comparison with the velocity profiles

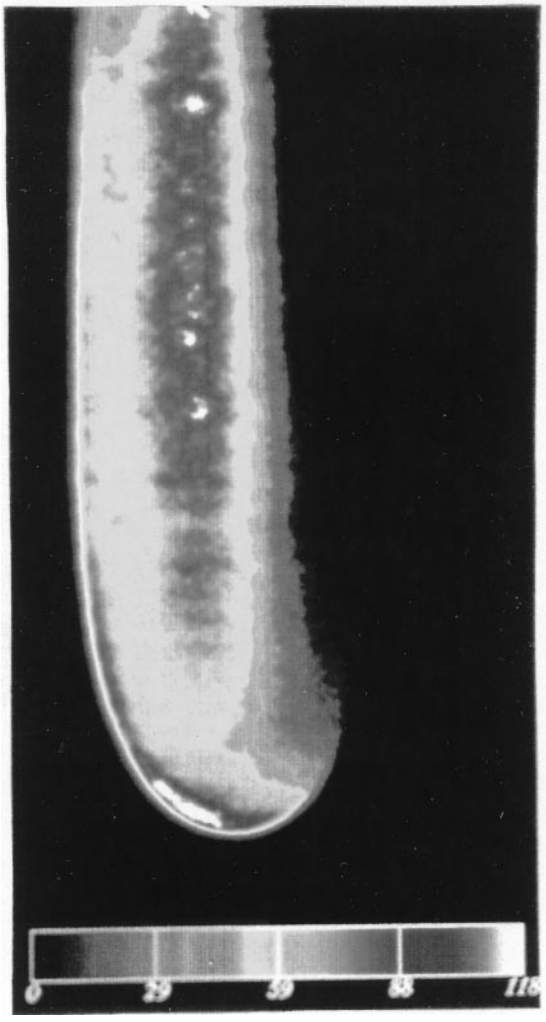

Fig. 2. Mean image of fluorescence of OH radicals in the triple flame of an unsaturated transition of species population at 308 nm.

obtained by hot-wire anemometry, velocity measurements were first made in non-reacting flow. It was found that for the PIV measurements there was a data scatter around the mean velocity of up to 7%. The size of the interrogation spots was at the least 1 times 1 mm. Consequently, changes which occurred in regions smaller than the spot size could not be resolved.

Experimental Results and Discussion

OH LIF results.

Shown in Fig. 2 is a fluorescence image of OH radicals after subtraction of the background image and subsequent normalization to eliminate the structures of the laser sheet and the collection optics. The frame of the image in physical space is 60 mm high and 35 mm wide. In the subsequent presentation, x and y denote the horizontal and the vertical axis, respectively, of a cartesian coordinate system whose origin is at the bottom left side corner. In the image of Fig. 2, the right side is the fuel rich side and the left side is the fuel lean side. From the image the following aspects are apparent: (i) the fluorescence of OH radicals is highest at the leading edge of the flame and attains a maximum value at the leading point, which, arguably, corresponds to the region of stoichiometric mixture and (ii) along the premixed parts of the flame the fluorescence of OH radicals drops rapidly away from the leading point. However, it drops faster, to a small value, along the rich premixed part than along the lean premixed part of the flame. Downstream of the leading edge of the flame, in the premixed parts of the flame and in the region between them and in the diffusion flame, the fluorescence intensity is much smaller on the rich premixed side than on the lean premixed side. This is well illustrated in the sectional plots shown in Fig. 3; (iii) a sectional plot at $x = 13$ mm (see Fig. 4) through the leading point of the flame and the diffusion flame, reveals that the fluorescence intensity rises sharply to a maximum value at the premixed flame front and then drops sharply before rising again to a plateau profile in the diffusion flame.

Note that the intensity of fluorescence in the diffusion flame is about the same as the maximum value in the premixed flame. The fluctuations appearing in the profiles presented above originate from noise in the imaging system. This includes the fluctuations in the structure of the laser beam. These fluctuations correspond to about 7% of the mean fluorescence. It is worth noting that the resolution of the arrangement here is 0.129 mm per pixel in both the vertical and the horizontal direction. Furthermore, during the period of 1 sec, in which a mean image is obtained, the movement of the flame was negligible as was established by evaluating the standard deviation of 200 images recorded over a period of 60 sec [12].

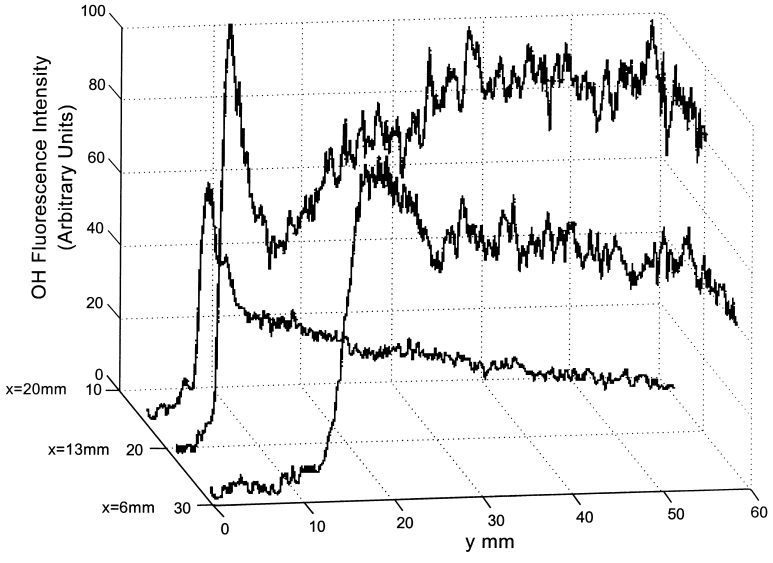

Fig. 3. Sectional plots in y-direction, for $x = 6$, 13, and 20 mm, of fluorescence intensity of OH radicals in triple flame of Fig. 2.

PIV results.

Photographic frames of particle image pairs (not shown here) are obtained using the double pulse illumination. The laser pulse separation time is chosen such that the distance between images in a pair in both the frozen flow region and the flame region is large enough for both regions to be interrogated in one setting of the interrogation equipment. This way inaccuracies, which would result from matching results of the two regions obtained from different frames or using different settings of the equipment, are eliminated.

Shown in Fig. 5 is a velocity vector plot processed from a photographic frame of particle image pairs. To further highlight the structure of the velocity field, superimposed on the vector plot are streamlines which have been traced into

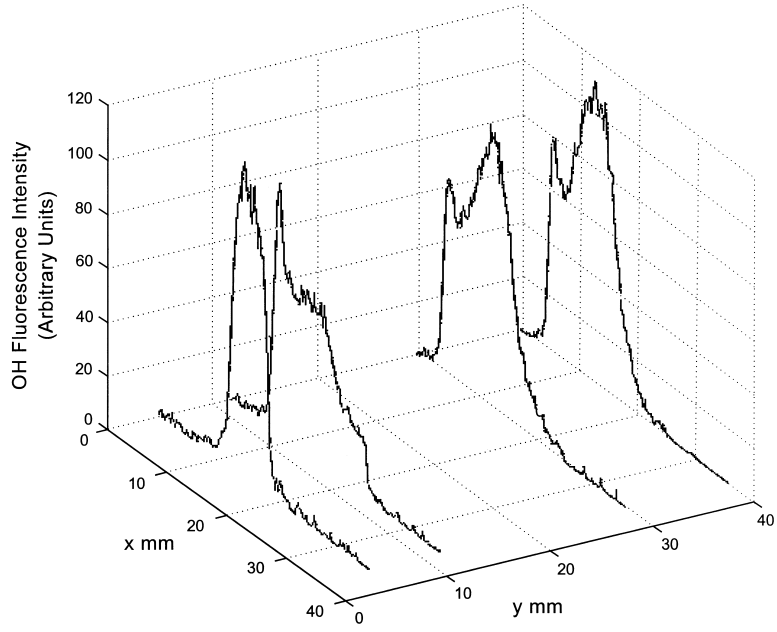

Fig. 4. Sectional plots in the x-direction, for $y = 5$, 12, 30, and 40 mm, of fluorescence intensity of OH radicals in triple flame of Fig. 2.

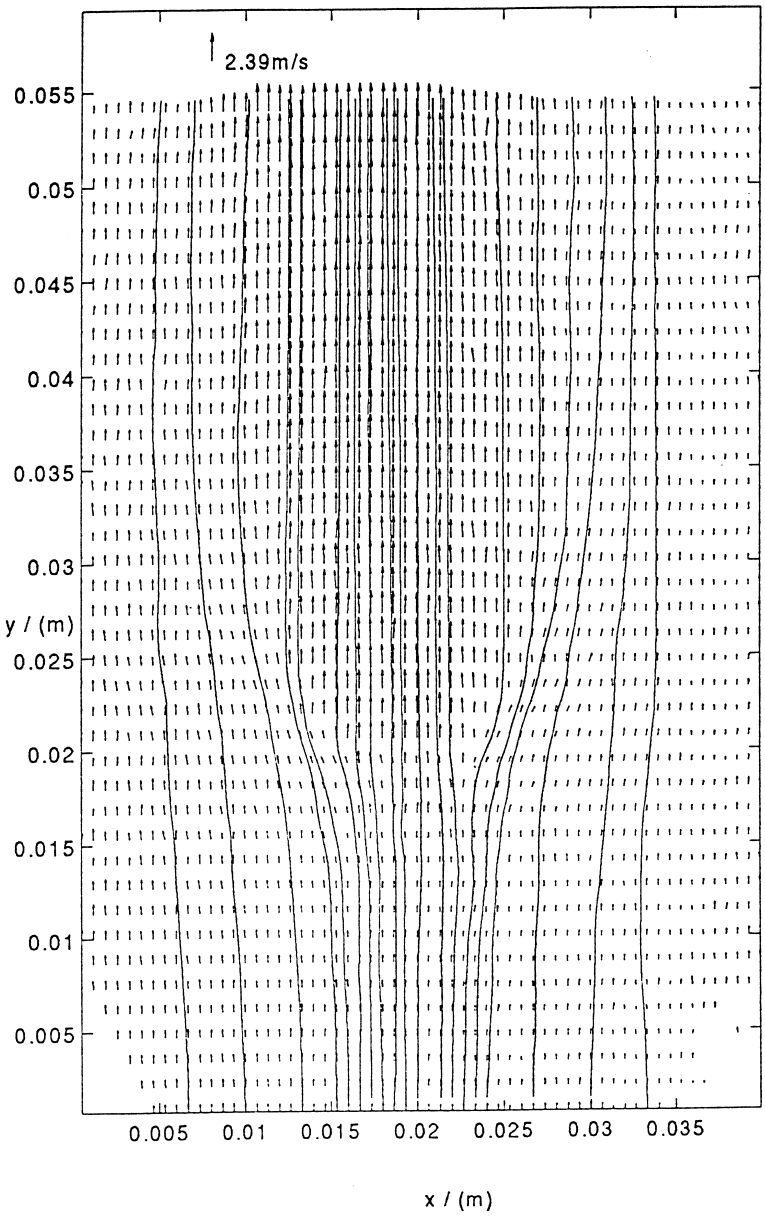

Fig. 5. Streamlines superimposed on PIV velocity vector plot.

the interrogation domain from the inlet of the frame using the Runge-Kutta-Mersion integration procedure. In the integration, temporal step sizes are chosen such that, in comparison to the PIV experimental errors, those of numerical integration are negligible.

From the PIV figures the following aspects are apparent:

(i) As expected, there is acceleration of the flow crossing the premixed parts of the flame. In addition, the maximum velocity occurs at the centre of the flame region approximately at the location of the diffusion flame. This is illustrated in Fig. 6, where velocities taken from the vector plot shown in Fig. 5 are plotted in the x-direction (transverse direction) at axial stations $y = 0.0466$ and 0.0133 m, respectively. It is seen that further downstream of the leading edge of the flame the velocity of the burnt gases increases.

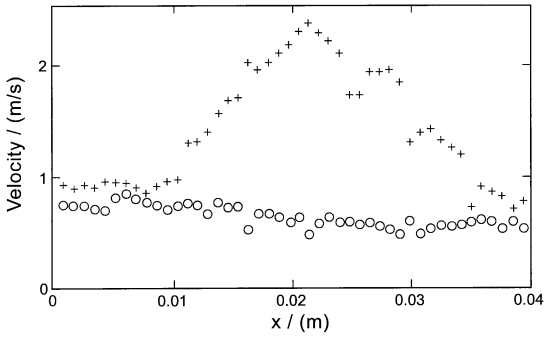

Fig. 6. Velocity profiles in x-direction at $y = 0.0466$ m (plus signs) and 0.0133 m (circles) of vector plot shown in Fig. 5.

(ii) The streamlines in Fig. 5 reveal that upon crossing the premixed flame front the flow is generally parallel to the y-axis.

(iii) There is a divergence of the flowfield upstream of the flame. Shown in Fig. 7 is the velocity along a streamline passing approximately through the leading point of the flame. The velocity is lowest in the region just upstream of the leading edge of the flame.

NUMERICAL STUDIES

Governing Equations and Boundary Conditions

In the governing equations, the independent variables are the time t and the coordinates x and y. Although steady-state solutions are sought, in the equations the time-derivative terms are retained because the numerical-solution algorithm adopted is based on a time-dependent approach to a steady-state solution.

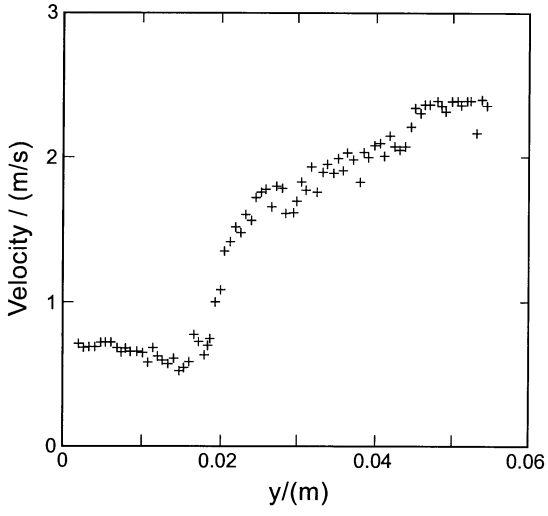

Fig. 7. Velocity along a streamline which passes approximately through the leading point of triple flame.

For convenience of presentation, in each equation the accumulative, convective and diffusive terms are grouped together in a generalized operator L, defined as

$$L(\phi;\,\Gamma_\phi) \equiv \frac{\partial(\rho\phi)}{\partial t} + \frac{\partial(\rho u\phi)}{\partial x} + \frac{\partial(\rho v\phi)}{\partial y} - \frac{\partial}{\partial x}\left(\Gamma_\phi \frac{\partial\phi}{\partial x}\right) - \frac{\partial}{\partial y}\left(\Gamma_\phi \frac{\partial\phi}{\partial y}\right).$$

Here ϕ represents any of the dependent variables ρ, u, v, T, or Y_i, $i = 1, \ldots, N$, and Γ_ϕ is the respective diffusion coefficient to be specified; ρ is the density of the gas mixture, and u and v are the velocity components in the x and y direction, respectively, T is the temperature, and Y_i denotes the mass fraction of species i. Thus, in terms of the operator L, the conservation equations can be written in the standard form

$$L(\phi;\,\Gamma_\phi) = S_\phi, \tag{2}$$

where S_ϕ represents a "source term" for the dependent variable ϕ. Specifically, the continuity equation is written as

$$L(1;\,0) = 0, \tag{3}$$

the x-momentum equation as

$$L(u;\,\mu) = -\frac{\partial p}{\partial x} + \rho g_x + \frac{\partial}{\partial x} \cdot \left\{\mu\left[\frac{\partial u}{\partial x} - \frac{2}{3}(\nabla\cdot\boldsymbol{v})\right]\right\} + \frac{\partial}{\partial y}\left(\mu\frac{\partial v}{\partial x}\right), \tag{4}$$

the y-momentum equation as

$$L(v;\,\mu) = -\frac{\partial p}{\partial y} + \rho g_y + \frac{\partial}{\partial y} \cdot \left\{\mu\left[\frac{\partial v}{\partial y} - \frac{2}{3}(\nabla\cdot\boldsymbol{v})\right]\right\} + \frac{\partial}{\partial x}\left(\mu\frac{\partial u}{\partial y}\right), \tag{5}$$

the energy equation as

$$c_p L(T;\, \lambda/c_p) = (\nabla T) \sum_{i=1}^{N} c_{pi}(\rho D_i \nabla Y_i) - \sum_{i=1}^{N} h_i w_i + H \qquad (6)$$

and the species-mass equations as

$$L(Y_i;\, \rho D_i) = w_i, \qquad (7)$$

$i = \Delta, \ldots, N$. Closure of the system of Eqs. (3–7) is achieved through the ideal-gas equation of state

$$\frac{p}{\rho} = R^0 T \sum_{i=1}^{N} \left(\frac{Y_i}{W_i}\right). \qquad (8)$$

In Eqs. (4) and (5), the divergence $\nabla \cdot \boldsymbol{v}$ of the velocity vector $\boldsymbol{v}$ is given by

$$\nabla \cdot \boldsymbol{v} = \frac{\partial u}{\partial x} + \frac{\partial v}{\partial y},$$

and in Eq. (6) the quantity H is defined as

$$H = \frac{\lambda}{c_P}\left[\frac{\partial T}{\partial x}\frac{\partial c_p}{\partial x} + \frac{\partial T}{\partial y}\frac{\partial c_p}{\partial y}\right]. \qquad (9)$$

Low Mach-number flow is considered. Therefore, in Eq. (6) effects of viscous dissipation are neglected and in Eq. (8) the pressure is taken as constant. In Eqs. (4) and (5), μ represents the dynamic viscosity of the gas mixture; the bulk viscosity is neglected. In Eq. (7), Fick's law of diffusion is used with suitably defined diffusion coefficients; Soret effects, Dufour effects, and pressure gradient diffusion are neglected. Details of the transport model including the formulation of the diffusion fluxes can be found in [14]. Symbols, which have not been defined explicitly, have their usual meaning.

A numerical solution of the above governing equations requires suitable boundary conditions to be specified. At the burner inlet, the profiles of all variables are assumed to be known and, therefore, Dirichlet boundary conditions are applied. The burner outlet is assumed to be physically sufficiently far from the region of interest for the assumption to be made that the gradients normal to the outlet of velocity components, temperature and species mass fractions are zero. At the walls, no-slip conditions are applied; thus, $u = v = 0$ at a wall. It is assumed that the walls are adiabatic and impermeable to matter and that, therefore, normal to each wall the gradients of temperature and species mass fractions are zero.

Solutions are sought for low Mach number flows and hence the pressure field is important only insofar as it affects the velocity field. The momentum boundary conditions are applied to a pressure equation in such a way as to reflect a physically realistic representation of the flowfield at the boundaries; for details [12] should be consulted.

Numerical Scheme

The purpose of the numerical modelling is to simulate a triple flame propagating in a flowfield similar to that realized experimentally. To predict the structure of the entire flowfield in detail solutions are sought for the full set of governing equations as presented in the prior section. In particular, the simulation is performed in two space coordinates because simplifying transformations into a single space coordinate are unsuitable. To cope with the nonrectangular physical domain, in which the flame is established in the experiment, the system of the governing equations is transformed with respect to the spatial coordinates onto a system of generalized curvilinear coordinates [12]. In the framework of this transformation, using a finite-volume technique, the system of governing equations is discretized on a collocated grid. The discretized governing equations are solved with the PISO algorithm [15]. The implementation of this algorithm is discussed in detail in [12]. To cope efficiently with the steep profiles of the dependent variables, following the practice in the computer code RUN-1DL [16], adaptive gridding [11, 12] is implemented to adaptively redistribute grid points and concentrate them, as the solution evolves, where they are needed most urgently, in regions of steep gradients and strong curvature of dependent variables.

Problem Specification

Using the computer code, steady-state solutions are sought for a triple flame propagating freely

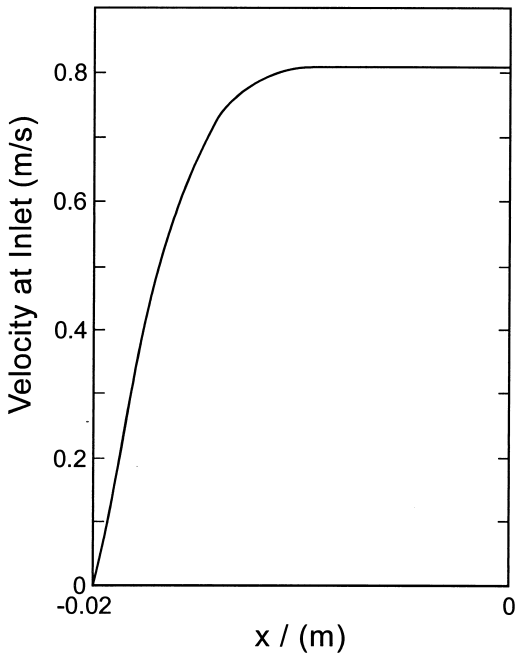

Fig. 8. Left half of symmetrical velocity profile specified at inlet to computational domain.

in a mixing layer. The inlet boundary conditions specified correspond to a case studied in the experimental work. The physical domain is a diverging channel, which is 400 mm long, of width 40 mm at the burner inlet and of width 72 mm at the burner outlet. The flow direction is upwards and buoyancy terms are included. Profiles are specified at the burner inlet for the velocity components, the temperature and the species mass fractions. For the y-velocity component a symmetrical top hat velocity profile, the left half of which is shown in Fig. 8, is specified; the x-velocity component is taken as zero. The species mass fractions profiles specified at the inlet are shown in Fig. 9.

Computational Procedure

The computational procedure consists of three steps: (i) use of a flame sheet model to generate the initial estimates for the scalar variables, (ii) use of finite rate chemistry based on a global one-step reaction to improve the results obtained from the flame-sheet model, and (iii) detailed chemistry calculations. Details of the transport coefficients and the thermodynamic data, as well as of the one-step reaction model, can be found in [12]. The chemical kinetic mechanism for methane used in the modelling of the flame with detailed chemistry is given in Table 1. The quantities A, n, and E in the last three columns of the table are the pre-exponential factor, the exponent of the pre-exponential temperature dependence and the activation energy, respectively, of the individual elementary reactions. The mechanism consists of chemical reactions of species with a maximum of one carbon atom and therefore comprises 17 chemical species. It has been extracted from a detailed mechanism of hydrocarbon fuels up to propane given in [17].

Since the numerical scheme employs a transient approach to the steady-state solution of the problem, the transient problem is computed for a real

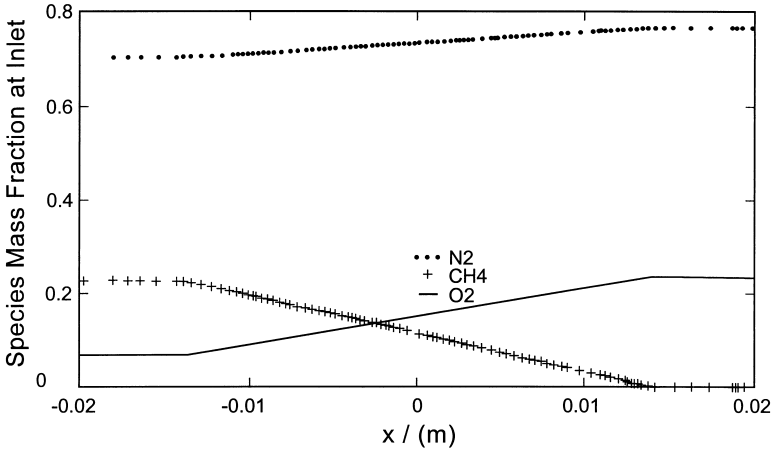

Fig. 9. Species mass fraction profiles at inlet to computational domain.

TABLE 1

Detailed Chemical Kinetic Mechanism for Methane/Air Systems

No.	Reaction	A mole, cm^3, sec	n	E kJ/mole
1	$O_2 + H \rightarrow OH + O$	2.000E+14	0.00	70.30
2	$OH + O \rightarrow O_2 + H$	1.568E+13	0.00	3.52
3	$H_2 + O \rightarrow OH + H$	5.060E+04	2.67	26.30
4	$OH + H \rightarrow H_2 + O$	2.222E+04	2.67	18.29
5	$H_2 + OH \rightarrow H_2O + H$	1.000E+08	1.6	13.80
6	$H_2O + H \rightarrow H_2 + OH$	4.312E+08	1.6	76.46
7	$OH + OH \rightarrow H_2O + O$	1.500E+09	1.14	0.42
8	$H_2O + O \rightarrow OH + OH$	1.473E+10	1.14	71.09
9	$O_2 + H + M' \rightarrow HO_2 + M'$	2.300E+18	−0.80	0.0
10	$HO_2 + M' \rightarrow O_2 + H + M'$	3.190E+18	−0.80	195.39
11	$HO_2 + H \rightarrow OH + OH$	1.500E+14	0.0	4.20
12	$HO_2 + H \rightarrow H_2 + O_2$	2.500E+13	0.0	2.90
13	$HO_2 + OH \rightarrow H_2O + O_2$	6.000E+13	0.0	0.0
14	$HO_2 + H \rightarrow H_2O + O$	3.000E+13	0.0	7.20
15	$HO_2 + O \rightarrow OH + O_2$	1.800E+13	0.0	−1.70
16	$HO_2 + HO_2 \rightarrow H_2O_2 + O_2$	2.500E+11	0.0	−5.20
17	$OH + OH + M' \rightarrow H_2O_2 + M'$	3.250E+22	−2.0	0.0
18	$H_2O_2 + M' \rightarrow OH + OH + M'$	1.692E+24	−2.0	202.29
19	$H_2O_2 + H \rightarrow H_2O + OH$	1.000E+13	0.0	15.0
20	$H_2O_2 + OH \rightarrow H_2O + HO_2$	5.400E+12	0.0	4.20
21	$H_2O + HO_2 \rightarrow H_2O_2 + OH$	1.802E+13	0.0	134.75
22	$H + H + M' \rightarrow H_2 + M'$	1.800E+13	−1.0	0.0
23	$OH + H + M' \rightarrow H_2O + M'$	2.200E+22	−2.0	0.0
24	$O + O + M' \rightarrow O_2 + M'$	2.900E+17	−1.0	0.0
25	$CO + OH \rightarrow CO_2 + H$	4.400E+06	1.50	−3.10
26	$CO_2 + H \rightarrow CO + OH$	4.956E+08	1.50	89.76
27	$CH + O_2 \rightarrow CHO + O$	3.000E+13	0.0	0.0
28	$CO_2 + CH \rightarrow CHO + CO$	3.400E+12	0.0	2.9
29	$CHO + H \rightarrow CO + H_2$	2.000E+14	0.0	0.0
30	$CHO + OH \rightarrow CO + H_2O$	1.000E+14	0.0	0.0
31	$CHO + O_2 \rightarrow CO + HO_2$	3.000E+12	0.0	0.0
32	$CHO + M' \rightarrow CO + H + M'$	7.100E+14	0.0	70.30
33	$CO + H + M' \rightarrow CHO + M'$	1.136E+15	0.0	9.97
34	$CH_2 + H \rightarrow CH + H_2$	8.400E+09	1.50	1.40
35	$CH + H_2 \rightarrow CH_2 + H$	5.830E+09	1.50	13.08
36	$CH_2 + O \rightarrow CO + H + H$	8.000E+13	0.0	0.0
37	$CH_2 + O_2 \rightarrow CO + OH + H$	6.500E+12	0.0	6.30
38	$CH_2 + O_2 \rightarrow CO_2 + H + H$	6.500E+12	0.0	6.30
39	$CH_2O + H \rightarrow CHO + H_2$	2.500E+13	0.0	16.70
40	$CH_2O + O \rightarrow CHO + OH$	3.500E+13	0.0	14.60
41	$CH_2O + OH \rightarrow CHO + H_2O$	3.000E+13	0.0	5.0
42	$CH_2O + M' \rightarrow CHO + H + M'$	1.400E+17	0.0	320.00
43	$CH_3 + H \rightarrow CH_2 + H_2$	1.800E+14	0.0	63.00
44	$CH_2 + H_2 \rightarrow CH_3 + H$	3.680E+13	0.0	44.30
45	$CH_3 + H \rightarrow CH_4$ (k_∞)	2.108E+14	0.0	0.0
	$CH_3 + H \rightarrow CH_4$ (k_0)	6.257E+23	−1.80	0.0
46	$CH_3 + O \rightarrow CH_2O + H$	7.000E+13	0.0	0.0
47	$CH_3 + O_2 \rightarrow CH_2O + OH$	3.400E+11	0.0	37.40
48	$CH_4 + H \rightarrow CH_3 + H_2$	2.200E+04	3.0	36.60
49	$CH_3 + H_2 \rightarrow CH_4 + H$	8.391E+02	3.0	34.56
50	$CH_4 + O \rightarrow CH_3 + OH$	1.200E+07	2.10	31.90
51	$CH_4 + OH \rightarrow CH_3 + H_2O$	1.600E+06	2.10	10.30
52	$CH_3 + H_2O \rightarrow CH_4 + OH$	2.631E+05	2.10	70.92

time duration which is sufficient for a steady-state solution to be achieved. The mesh is progressively adapted to the evolving flame structure.

The flame sheet model predicts a combustion region that starts at the inlet of the computational domain. Then, using finite rate chemistry based on a global one-step reaction, the temperature and the species mass fraction are gradually adjusted from the profiles of the flame sheet model. Subsequently, the inlet velocity is increased in order to lift the flame off from the inlet, further into the computational domain. Finally, the solution obtained with the global one-step reaction is taken as the initial guess to start the more detailed computations. The initial mass fractions of additional species, which are not present in the one-step reaction, have been obtained on the basis of a mixture fraction variable for a one-dimensional solution for a methane-air diffusion flame in a counterflow geometry. First computations are for all dependent variables except the temperature, which is initially held constant until reasonably good and stable solutions of the other variables have been obtained. Then the temperature field is released and solutions are sought for all the dependent variables.

Numerical Results and Discussion

Shown in Fig. 10 is a plot of streamlines through the flame. As expected, far ahead of the flame, in the streamwise direction, streamlines diverge and hence the velocity decreases as a result of the increasing cross-sectional area of the diverging channel. In the region just upstream of the flame the flow diverges significantly more. Across the flow cross section in this region the velocity is larger at the periphery and decreases towards the streamline passing through the leading point of the flame. Shown in Fig. 11 is the velocity magnitude along a streamline which passes approximately through the leading point of the flame. The minimum velocity occurs just before the streamline enters the preheat zone.

Upon entering the transport zone, and hence the flame, there is, as expected, a sudden acceleration to a maximum velocity which is attained well within the flame. The minimum velocity attained just ahead of the flame is approximately equal to the burning velocity of a stoi-

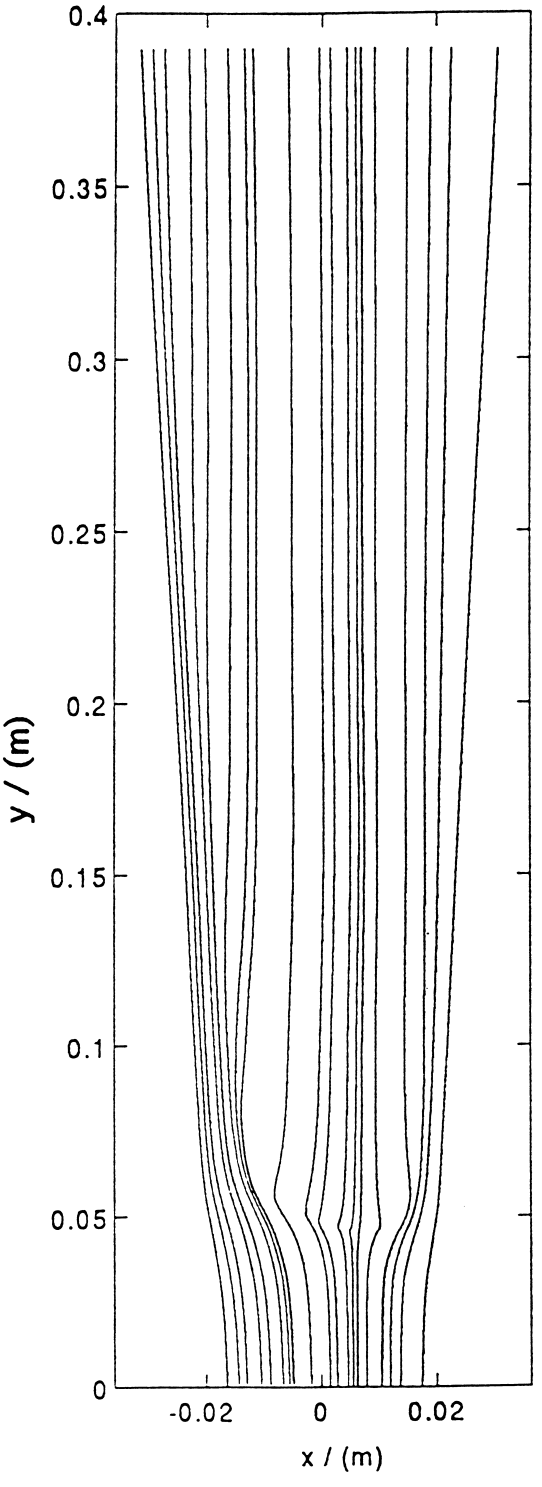

Fig. 10. Plot of streamlines from numerical solution for velocity field.

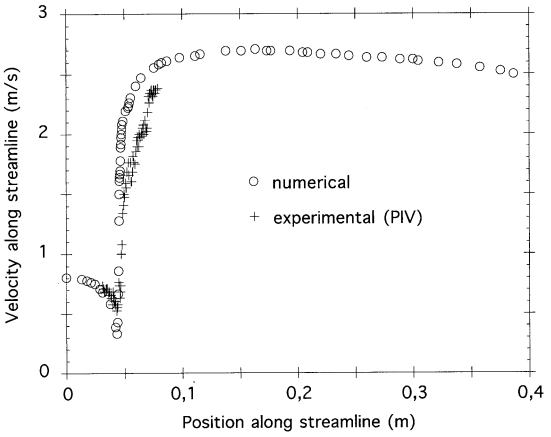

Fig. 11. Velocity magnitude along a streamline through leading point of the triple flame. Circles: numerical data, plus signs: PIV data.

chiometric fuel-air mixture. Furthermore, the leading point is approximately located in a region of stoichiometric mixture.

Shown in Fig. 12 are the contours of isotherms. These lie close together in the region of the premixed flame, which is where most of the combustion takes place. The maximum temperature attained is 1992 K at the triple point. Although the channel is divergent and the flame is not symmetrically located in it, in the region of hot gases the isotherms and the streamlines are aligned with the direction of gravity, thus showing the effects of buoyancy. Figures 13 and 14 show plots of the mass fractions of methane and oxygen, respectively.

Shown in Fig. 15 is a qualitative contour plot of the heat release rate clearly exhibiting the structure of a triple flame. In the figure, the lean premixed flame is on the right, the rich premixed flame is on the left, with the diffusion flame in the middle. The heat release rate attains the highest value in the premixed flame at the leading edge. It has a generally high value in the leading part of the flame, which is in a nearly normal orientation to the mean direction of flow. Note that the heat release rate in the trailing diffusion flame is very low compared to the heat release rate in the premixed flames.

Figure 16 shows qualitative contours of the mass fraction of OH in the flame. There is a high concentration of OH in the premixed flame wings. However, this drops behind the wings and then rises again in the diffusion flame. The

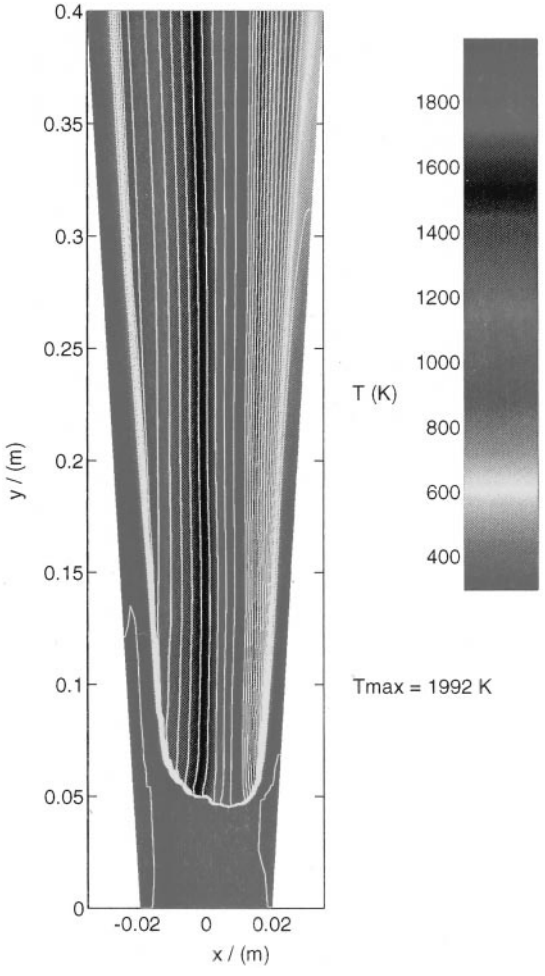

Fig. 12. Contour plot of temperature.

concentration of hydroxyl radicals in the diffusion flame is much larger than in the premixed flame. Generally the concentrations of radicals are found to be much higher on the lean premixed side than on the rich premixed side of the flame. The concentration of CO (not shown here) attains a maximum value in the premixed flame. The level of CO in the diffusion flame is low. Furthermore, there is a higher concentration of CO on the rich side than on the lean side.

COMPARISON OF EXPERIMENTAL AND NUMERICAL RESULTS

Velocity Field and Natural Luminosity of the Flame

It is evident in the streamline plots shown in Figs. 5 and 10 that the structures of the velocity

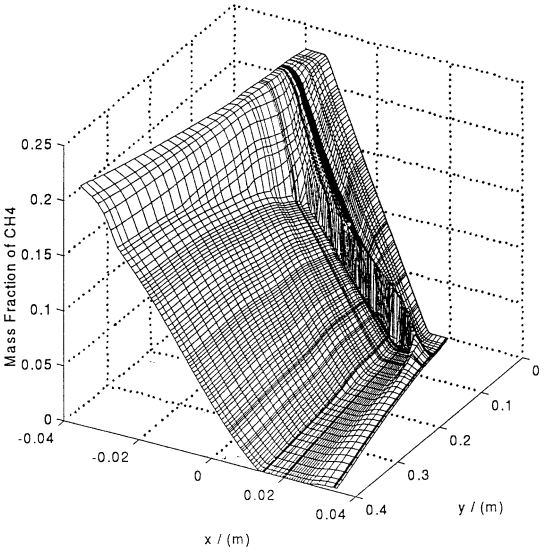

Fig. 13. Mesh plot of mass fraction of CH_4.

fields determined experimentally and numerically, respectively, are similar. Specifically, we note the agreement in the divergence of the flowfield ahead of the triple region, the deflection of the streamlines towards the centre of the flame upon crossing the flame surface, and the subsequent parallel flow. The streamlines passing through the triple region are approximately normal to the flame surface and therefore they undergo only a small change in direction upon crossing the flame. The velocity change along

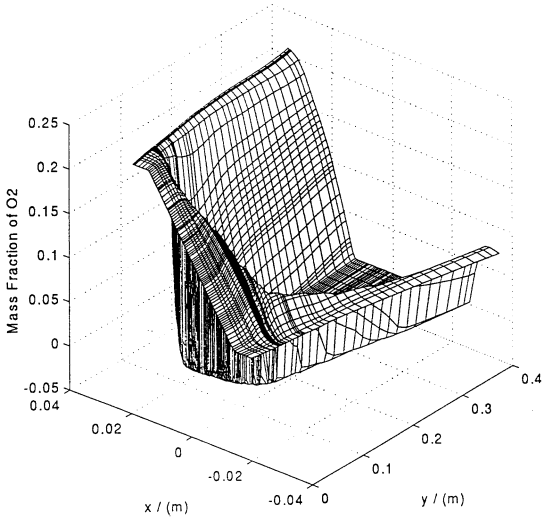

Fig. 14. Mesh plot of mass fraction of O_2.

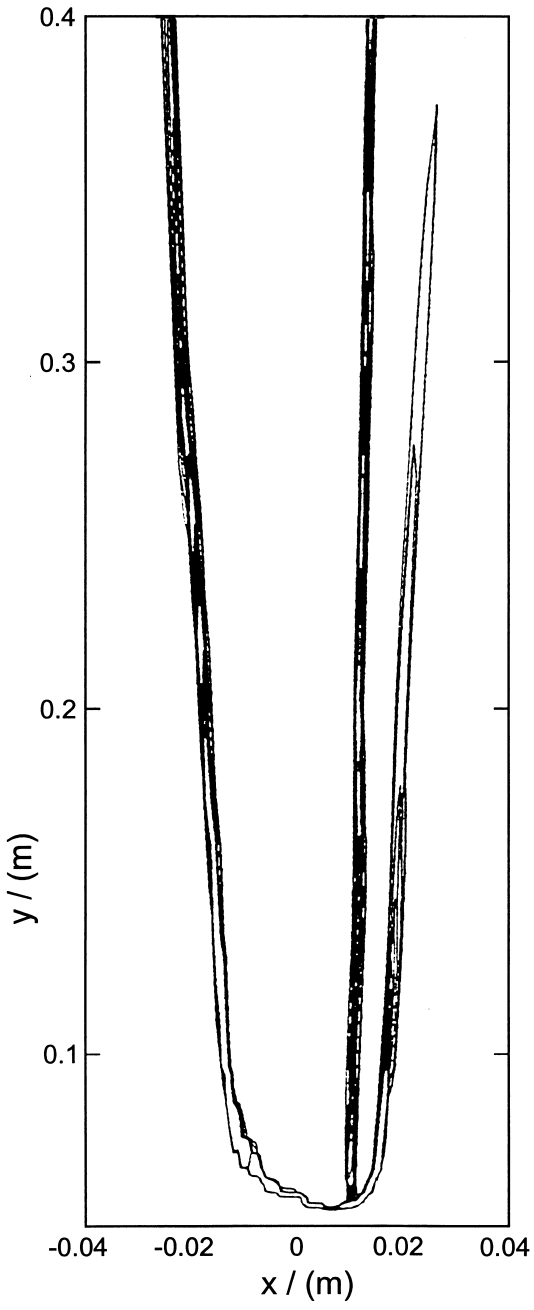

Fig. 15. Contour plot of heat-release rate.

these streamlines manifests a relationship between the upstream velocity field and the burning velocity. The minimum velocity along such streamlines, shown in Figs. 7 and 11 for the experimental and the numerical results, are 0.42 m/s and 0.34 m/s, respectively. For purposes of

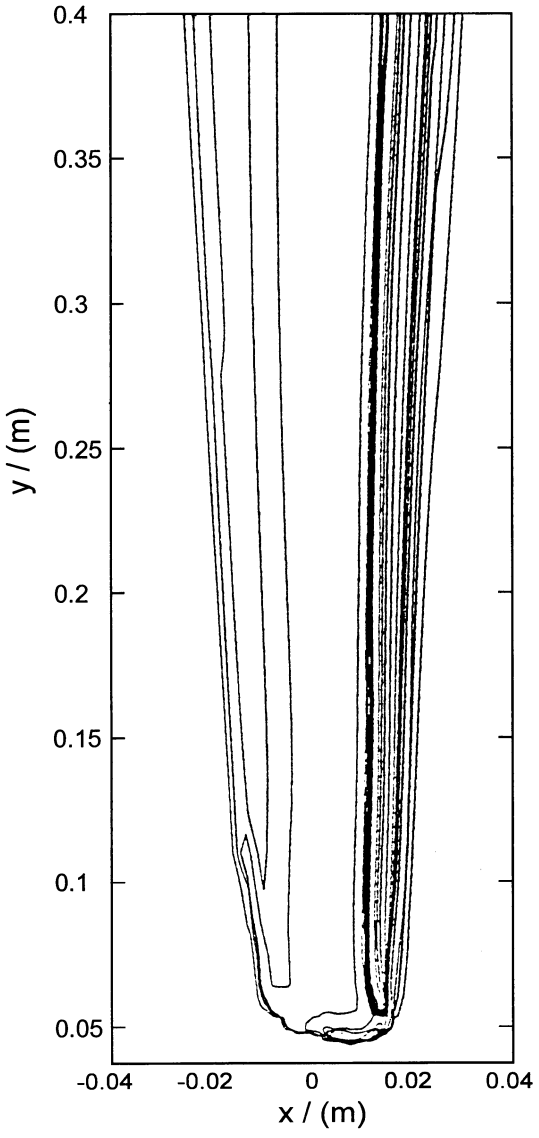

Fig. 16. Contour plot of the mass fraction of OH.

comparison, Fig. 11 shows numerical (circles) and experimental data. To facilitate comparison, the two plots have been matched at the leading edge of the flame.

In the computations a lower value than that obtained in the experimental measurements might be expected because in the measurements there is a combined bias by the higher velocities on both sides of the region of minimum velocity, which is too narrow to be accurately resolved with the PIV technique. The maximum velocity occurs in the central region of the flame close to the triple region in both the numerical and the experimental results and was 2.71 and 2.37 m/s, respectively.

In the experimental work the triple flame structure is observed as a blue luminous region [11]. The blue light is radiated by chemical species, such as the hydroxyl radicals, whose concentrations decay quite rapidly away from the luminous zones. From LIF measurements, we note that large amounts of the OH radicals are generated in the diffusion flame. Furthermore, the region of the diffusion flame, where the radicals are generated, is separated from the premixed flame and has a very high concentration of radicals. In the numerical results, the triple flame manifests itself in the heat release rate, which clearly exhibits the two premixed-flame and the diffusion-flame branch (see Fig. 15).

OH Mass Fraction Field

Numerical data based on a detailed chemical kinetic mechanism show (Figs. 3, 16) that the predicted concentration field of the hydroxyl radicals agree, qualitatively, with that obtained by LIF measurements. It is noted that there is a decrease in the concentration of the hydroxyl radical in the triple region at the junction of the diffusion flame and the premixed flames. From the numerical data it is noted that in this region there is a high concentration of other species, such as CO, which are involved in reactions that consume the hydroxyl radicals. Since the divergence of the flowfield upstream of the leading edge of the flame leads for the mixture, which is close to stoichiometry, to a large reaction region, it is probable that the region immediately behind the premixed flame front at the region of stoichiometric mixture has very little oxidiser and fuel left for chemical reactions in which the hydroxyl radicals are generated. However, because of the high temperature in this region there is a high density of species, such as CO, which are involved in reactions that consume the hydroxyl radicals. This imbalance between the generation and the consumption of the hydroxyl radicals leads to the structure observed at the triple region.

Further downstream of this region the fuel and the oxidiser, diffusing from the periphery of

the flame from opposite sides, begin to reach the central part of the flame, and their reactions lead to a higher generation of the hydroxyl radical. Consequently, the triple flame obtained here consists of the premixed flames trailed, at a small distance from the region of stoichiometric mixture, by a diffusion flame. It follows that the distance between the diffusion and the premixed flames will decrease as the mixture fraction gradient is increased. If the gradient is increased further, all three flames merge at the so-called triple point.

CONCLUSIONS

A qualitative distribution map of the hydroxyl radicals in the flame has been obtained using planar LIF. For the case studied, the distribution of this radical shows that the diffusion flame trails the premixed flame front at a small distance from the region of stoichiometric mixture. In addition, the map shows a large disparity in the concentration of hydroxyl radical between fuel-rich and fuel-lean regions of the flame and, therefore, highlights the variations in the nature of the chemical reactions in the flame.

PIV measurements reveal a considerable modification of the structure of the velocity field upstream of the leading edge of the flame. The velocity just upstream of the leading edge of the flame is approximately equal to the burning velocity of the stoichiometric mixture.

The experimental findings are supported by results obtained from numerical Navier-Stokes simulations of the flame.

This project was carried out when one of the authors (P. N. K.) was on a scholarship, at Cambridge University, provided by Shell International through the Cambridge Commonwealth Trust. One of the authors (P. N. K.) would like to acknowledge the assistance of S. Harding and N. Tait in setting up the OH LIF equipment and also the fruitful discussions on PIV with N. H. Armstrong.

REFERENCES

1. Peters, N., *Twentieth Symposium (International) on Combustion*, The Combustion Institute, Pittsburgh, 1984, pp. 353–360.
2. Peters, N., *Twenty-first Symposium (International) on Combustion*, The Combustion Institute, Pittsburgh, 1986, pp. 1231–1250.
3. Liew, S. K., Bray, K. N. C., and Moss, J. B., *Combust. Flame* 56:199–213 (1984).
4. Rogg, B., Behrendt, F., and Warnatz, J., *Twenty-first Symposium (International) on Combustion*, The Combustion Institute, Pittsburgh, 1986, pp. 1533–1541.
5. Dold, J. W., Hartley, L. J., and Green, D., in *Dynamical Issues in Combustion Theory*, *IMA Volumes in Mathematics and its Applications* (P. C. Fife, A. Liñán, and F. A. Williams, Eds.), Springer Verlag, New York, 1990.
6. Phillips, H., *Tenth Symposium (International) on Combustion*, The Combustion Institute, Pittsburgh, 1965, pp. 1277–1283.
7. Liñán, A., and Crespo, A., *Combust. Sci. Technol*. 14:95–117 (1976).
8. Dold, J. W., in *Dynamics of Deflagrations and Reactive Systems: Flames*, *Vol. 131 of Progress in Astronautics and Aeronautics* (A. L. Kuhl, J. R. Bowen, J.-C. Leyer, and A. A. Borisov, Eds.), AIAA, New York, 1988, pp. 240–248.
9. Dold, J. W., *Combust. Flame* 76:71–88 (1989).
10. Dold, J. W., *Flame Propagation in a Mixing Layer*. Paper presented at the 3rd Int. Seminar on Flame Structure, September 1989.
11. Kĩoni, P. N., Rogg, B., Bray, K. N. C., and Liñán, A., *Combust. Flame* 94:276–290 (1993).
12. Kĩoni, P. N., *A Numerical and Experimental Study of the Structure of Laminar Triple Flames Propagating in Mixing Layers*, PhD thesis, Department of Engineering, University of Cambridge, 1994.
13. Armstrong, N. W. H., *Planar Flowfield Measurement in Premixed Turbulent Combustion*. PhD thesis, Department of Engineering, University of Cambridge, 1992.
14. Rogg, B., *Combust. Flame* 73:45–65 (1988).
15. Issa, R. I., *J. Comp. Phys*. 62:40–65 (1986).
16. Rogg, B., in *Reduced Kinetic Mechanisms for Applications in Combustion Systems* (N. Peters and B. Rogg, Eds.), Springer-Verlag, Berlin-Heidelberg, 1993, appendix C.
17. Peters, N., in *Reduced Kinetic Mechanisms for Applications in Combustion Systems* (N. Peters and B. Rogg, Eds.), Springer-Verlag, Berlin-Heidelberg, 1993, pp. 3–14.

Received 17 September 1996; revised 8 February 1998; accepted 8 March 1998